In Vivo Modeling of Biphasic Mechanics in the Brain: A Poroelastic Constitutive Model with Enhanced Structural Description Approach

By

Saramati Narasimhan

Thesis

Submitted to the Faculty of the

Graduate School of Vanderbilt University

in partial fulfillment of the requirements

for the degree of

MASTER OF SCIENCE

in

Biomedical Engineering

December 16, 2017

Nashville, Tennessee

Approved:

Michael I. Miga, Ph.D.

Logan Clements, Ph.D.

ACKNOWLEDGEMENTS

This work would not be possible without the contributions from Dr. Jared A. Weis, Hernán F. J. González, Reid C. Thompson, and Michael I. Miga. I would also like to thank Professor B. Dawant and Dr. Logan Clements for their helpful discussions during the course of this study. Dr. Logan Clements also served as the second reader for this thesis. We would also like to thank Professor of Surgery, P. Jack Hoopes, DVM, Ph.D. from Geisel School of Medicine, Dartmouth College for his assistance in generating the original data used in this thesis. This work was supported by the NIH-National Institute of Neurological Disorders and Stroke R01NS049251, and the NIH Training Grant T32 EB021937.

TABLE OF CONTENTS

LIST OF TABLES

LIST OF FIGURES

CHAPTER I

INTRODUCTION

The appropriate modeling of the biomechanics of the brain for use in interventional applications has significant clinical implications. It has the potential to provide noninvasive prediction of therapy delivery (Dai et al., 2016), reduce intraprocedural imaging requirements (Chen et al., 2011), and potentially reduce unnecessary procedures (Miga, 2016). One such application is image-guided neurosurgery (IGNS) (Schulz et al., 2012). During neurosurgery, the brain shifts due to a variety of intraprocedural factors such as swelling, hyperosmotic drugs, and/or changes in cerebrospinal fluid levels (Sun et al., 2014). As a result, the patient anatomy represented in the preoperative imaging no longer matches the intraoperative presentation and compromises the navigation information provided via IGNS. An accurate prediction of brain deformation could allow systems to be constructed that could compensate for intraoperative brain shift and reestablish alignment fidelity during IGNS (Miga et al., 2016), (Nimsky et al., 2000), (Ohue et al., 2010). While the previous example is primarily concerned with tissue localization, another application heavily dependent on understanding brain biomechanics is convection enhanced delivery (CED). In this case, the important goal is to understand how drug is distributed in the brain via direct interventional catheter. While still having aspects of localization central, this has a wider concern about the distribution and extent of a delivered drug therapy within the tissue. In the example of CED, modeling could be used to more accurately forecast the drug delivery and as a means to optimize convection parameters and consequently enhance treatment (Lieberman et al., 1995), (Linninger et al., 2008), (Raghavan et al., 2006). Each of these applications are clinically distinct treatments but are intrinsically linked in soft-tissue brain biomechanics.

The brain itself is a highly complex organ with a variety of physical structures. In addition, brain tissue exhibits properties of heterogeneity and anisotropy. Historically, the Monro-Kellie doctrine has been a central working description of brain biomechanics which states that the cranial cavity is a fixed volume that is the sum of the volumes of brain tissue, intracranial blood, and cerebrospinal fluid (CSF) (Monro, 1783). It naturally follows that with an increase in one of the components, there must be a decrease in one of or both of the other (Monro, 1783). Treating the brain as only a solid tissue (often the case in brain models) negates the inherently biphasic nature of the brain within the cranial environment. In addition to these constitutive components, the anatomical geometric configuration of the brain is also quite complex. The brain is encapsulated by the dura, which is a fibrous membrane (Siegel and Sapru, 2015). The dura extends into folds of the brain forming the dural septa, which consist of the falx cerebri and the tentorium cerebelli; the dural septa serve the purpose of reducing brain displacements during motion (Siegel and Sapru, 2015). The falx cerebri partially separates the cerebral hemispheres, and the tentorium cerebelli separates the occipital lobes and the cerebellum (Siegel and Sapru, 2015). The pattern on the surface of the brain consists of sulci and gyri. The sulci are the groves in the brain, and the gyri are the plateaus formed by the boundary ridges of sulci pairs (Siegel and Sapru, 2015). There are also the four connected ventricular cavities present within the brain to consider as well. These cavities are filled with CSF, and they are connected to the central canal within the spinal cord and the space around the brain (Siegel and Sapru, 2015). Intracranial pressure is the pressure measured within the cranial vault (Freeman, 2015). Experimental evidence suggests that intracranial pressure can vary spatially within the brain. This was previously suggested in a porcine study in which an extradural temporal mass lesion was simulated with an epidural balloon (Wolfla et al., 1997). Separate but similar experiments with an expanding frontal mass also reported similar findings (Wolfla et al., 1996).

In addition to a complex geometry, brain tissue consists of both grey and white matter. Grey matter consists mostly of cell bodies, and white matter is mainly nerve fibers (Siegel and Sapru, 2015). Quantifying the properties of brain tissue is necessary for accurately modeling the biomechanics of the brain. There have been attempts to quantify the material properties associated with these tissues. One approach, used in multiple studies, was to attempt to quantify these properties using magnetic resonance elastography (Green et al., 2008), (Sack et

al., 2008). Another group attempted to quantify the large strain properties of grey and white matter in rectangular tissue samples undergoing shear testing (Prange and Margulies, 2002). A separate, *in vitro,* study quantified samples of swine brain tissue in uniaxial tension (Miller and Chinzei, 2002). These studies and many others, which range from *in vitro* to *in vivo* testing, vary in protocols and in results (Chatelin et al., 2010). These inconsistent property values obtained in these many studies have led to variability within existing biomechanical modeling techniques. With respect to the exchange with interstitial fluid spaces within brain tissue, grey matter is not easily distorted and typically only changes its fluid content by approximately 1.5%, whereas, white matter has a much more compliant structure and can increase by as much as 10% (Doczi, 1993).

There is an extensive history of using computational models in a patient specific manner (Clatz et al., 2005), (Coffey et al., 2013), (Miga et al., 1997), (Miller and Chinzei, 1997), (Mostayed et al., 2013), (Sun et al., 2014). Despite extensive research done on the subject of biomechanical modeling of the brain, there is still not a general consensus on what representation should be used (Gerard et al., 2017), (Kyriacou et al., 2002), (Miga, 2016), (Wittek et al., 2009). Model types include viscoelastic (Hagemann et al., 2002), (Miller, 1999), poroelastic (Miga et al., 2001), (Paulsen et al., 1999), elastic (DeLorenzo et al., 2012), (Ferrant et al., 2002), and hyperelastic (Karami et al., 2009), (Wittek et al., 2009) models. Evidence for all these model types have been provided by many research groups in various clinical applications. In this work, we continue to investigate a poroelastic model which treats the brain as a material consisting of both an elastic solid matrix and a fluid component. We suggest this biphasic representation is in better agreement with the observations that led to the Monro-Kellie Doctrine. Going further, with respect to enhanced anatomical modeling, some work has been accomplished. One group used an inhomogeneous patient-specific model of the brain (Hu et al., 2007). In another investigation, improvements in subsurface shift were found in seven clinical cases by accounting for the dural septa (Chen et al., 2011). Another group investigated the influence of CSF boundaries and hippocampal fissures on convection enhanced delivery simulations. They concluded through simulations that the presence of fissures in the model influenced their simulation results (Dai et al., 2016). These investigations, and others like them, point towards the significance of accounting for the geometry of the brain. Ultimately, the predominant reason for variations in representation, both constitutive and geometric, arises from common investigational approaches that attempt to study soft-tissue in isolation rather than generating systems for *in vivo* observation. Unfortunately, this is a product of the extremely challenging nature of *in vivo* work and the deployment of instrumentation within that domain.

With this background in mind, we present three main contributions of this investigation. First, we demonstrate the ability to accurately model *in vivo* interstitial pressures in a porcine experiment using a poroelastic model. While this work does not validate the use of the poroelastic model in the brain in all applications per se, it does provide meaningful evidence for its consideration in the appropriate modeling of brain. The second contribution is a systematic investigation into the set of boundary conditions and mesh specifications, representative of anatomical characteristics of the brain, necessary to capture the behavior of the brain. Finally, a set of approximate values describing brain tissue material properties is provided.

CHAPTER II

METHODS

In Vivo Porcine Data

The *in vivo* data used for this investigation came from a porcine experiment done by Miga et al. (Miga et al., 2000). Miga et al. performed this study, approved by the Institution Animal Care and Use Committee at Dartmouth College, on a series of Yorkshire pigs from Parson's Farm, Hadley, MA (Miga et al., 2000). After being anesthetized, the porcine subject had pressure transducers (Johnson & Johnson Codman Microsensor ICP Transducer ~ Raynham, MA, Part No. 82-6631) implanted in the midbrain/frontal region of each hemisphere (Miga et al., 2000). One transducer is in the hemisphere ipsilateral to the simulated surgical load, explained below, while the other transducer is in the contralateral hemisphere. These sensors measured the interstitial pressures during the application of loading. Before any surgical procedure was performed on the porcine subject, an MR (magnetic resonance) of the neuroanatomy was acquired (Miga et al., 2000). In addition to the pressure transducers, 1 mm stainless steel beads were implanted into the parenchyma in a grid-like fashion in order to monitor brain tissue movement during the study (Miga et al., 2000) (note in (Miga et al., 2000), gross pathology was performed post-mortem to assess implant reactions, which were minimal). A temporal craniotomy was performed on the porcine subject, and a surgical-like load was applied through it against the intact dura with a piston-like source. This piston was attached to a stereotactic frame, and the piston was translated in increments of 2 and 4 mm (Miga et al., 2000). At the start of the experiment, a baseline CT (computed tomography) scan of the head was obtained. A CT scan was also performed after each piston translation, enabling the measurement of the bead displacement at the conclusion of each translation. The interstitial pressure was measured continuously during all piston translations. A more complete description of the protocols followed in this animal study can be found in the original paper located in the references (Miga et al., 2000). For the purposes of our investigation, the pressure and displacement data from three piston translations (8 mm, 10 mm, 12 mm) were used.

Biphasic Poroelastic Model

In this investigation, we are using a poroelastic model of the brain. This poroelastic model comes from Biot's description of consolidation theory (Biot, 1941) and has been extensively developed for brain biomechanics (Miga 1998). The governing equations of this model are:

$$\nabla \cdot G\nabla \boldsymbol{u} + \nabla \frac{G}{1-2v}(\nabla \cdot \boldsymbol{u}) - \alpha \nabla p = 0 \quad (1)$$

$$\alpha \frac{\partial}{\partial t}(\nabla \cdot \boldsymbol{u}) + \frac{1}{S}\frac{\partial p}{\partial t} - \nabla \cdot k\nabla p = 0 \quad (2).$$

The variables in (1) and (2) are identified in Table 1. Equation (1) relates mechanical equilibirum to the interstitial pressure gradient. Equation (2) relates volumetric strain to the conservation of fluid in a porous media.

The governing equations are solved using the Galerkin finite element method in 3-dimensions (3D) with linear tetrahedral elements (Lynch, 2005). The full weighted residual, finite element representation of (1) and (2) have been previously described (Paulsen et al., 1999). Fully implicit time stepping is required for temporal integration (Miga et al., 1998). The time step in the three piston pushes examined in the scope of this investigation is 90 *seconds*. The model is solved with a direct solver package, MUltifrontal Massively Parallel sparse direct Solver (MUMPS) (Amestoy et al., 2001), (Amestoy et al., 2006), and utilizes a sparse matrix library, Portable, Extensible Toolkit for Scientific Computation (PETSc) (Balay et al., 2016b), (Balay et al., 1997), (Balay et al., 2016a).

We generate two finite element meshes to perform this investigation, both representing the same porcine subject. We make the meshes by segmenting the porcine brain from the MR series taken during the animal study. A single

TABLE 1
EQUATIONS' VARIABLES

Symbol	MEANING	Units
p	Interstitial pressure	Pa
$\boldsymbol{u}$	Displacement vector	m
G	Tissue shear modulus ($G = E/2(1+v)$)	Pa
E	Young's modulus	Pa
v	Poisson's ratio	(unitless quantity)
α	Ratio of fluid volume extracted to volume change of tissue under compression	(unitless quantity)
$\frac{1}{S}$	Void compressibility constant (amount of fluid capable of being forced into a tissue constant in volume)	Pa^{-1}
k	Hydraulic conductivity	$(m^3s)/kg$

surface description of the brain with the ventricles is created using the marching cube algorithm from the manually segmented brains (Schroeder et al., 1996). Then a linear tetrahedral element mesh, visualized by the outer boundary of Fig. 1 is generated using a custom software based on the surface description (Sullivan et al., 1997). The CT and MR spaces are coregistered to one another, ensuring that the transducer and bead positions determined in measurement space (CT) are all located in computational model space (MR) (Miga et al., 2000). In order to represent the heterogeneity of brain matter, tetrahedral elements are classified according to the corresponding white and grey matter within an element from MR intensity (Miga et al., 2000), (Miga et al., 2000). This distinction is visualized in Fig. 1 in the axial slice through the mesh of the brain. Ventricles were treated as a separate structure and serve as an internal boundary capable of supporting presecribed boundary conditions. The vetricular boundary surface is illustrated by the black points within Fig. 1.

The single mesh, described above, captures grey matter, white matter, and ventricles. While this covers the heterogeneity of the brain tissue and venricular structure, it does not speak to the dural septa. The dural septa are accomplished by manually segmenting the falx cerebri and the tentorium cerebelli planes and using a custom splitting code that generates two neighbor nodes within the same spatial region. The dural septa split can be visualiazed within the image of the finite element mesh in Fig. 1. A series of meshes are created with and without septa to study its anatomical influence. The number of elements in the mesh is approximately 224,000 and the number of nodes for all meshes is over 40,000.

The value prescribed for both grey and white matter in all piston pushes are as follows. The Young's modulus is 2,100 Pa, and the value of Poisson's ratio is 0.45. Material properties associated with hydraulic conductivity (k) and the saturation constants (α, $\frac{1}{S}$), are the subject of material property determination for grey and white matter. These six material properties (k, α, $\frac{1}{S}$ for grey and white matter, respectively) are allowed to vary and are fit for in the inverse model (*Methods Section D*). We should also note that while Young's modulus and Poisson's ratio are likely modestly affected as well, we elected to use values that were previously determined

to optimize (Miga et al., 1998) with respect to a homogeneous model to reduce the degrees of freedom.

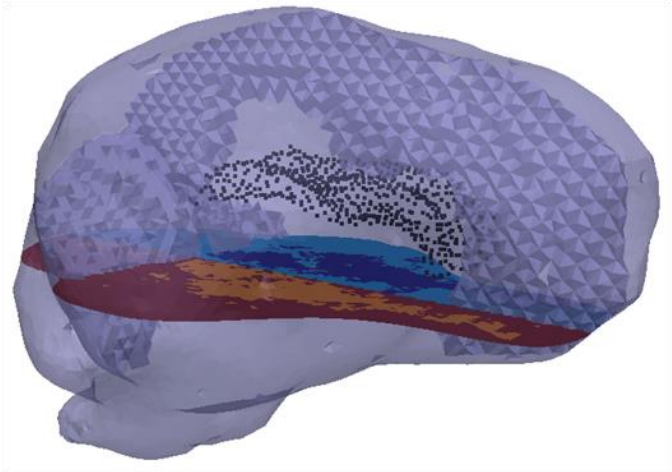

Figure 1. Finite element mesh representative of the porcine brain. The dural septa splits are discernable within the mesh. The black points within the mesh visualize the nodes of the boundary between the brain parenchyma and the ventricles. The slice through the mesh visualizes the distinction between grey and white matter within the parenchyma. There is an additional distinction, which is not enforced in this study, between the tissues in either hemisphere.

Our description of the mesh so far does not account for the gyri and sulci. These structures are present throughout the brain, and we hypothesize that these serve as a source of compliance in the brain and as such allowed for variability in our saturation constants, α, $\frac{1}{S}$. In the literature these are often prescribed as α=1, $\frac{1}{S} = 0$ indicating a fully saturated media (Chen et al., 2011), (Miga et al., 2000). While certainly intuitive, the propagation of pressure in the brain at the bulk level seems to contradict that behavior. This led to our approach suggesting that some of the finer fissure systems, not currently resolved, are acting as a source of compliance, much like the ventricular system does often in space occupying lesions.

Model Sensitivity

The purpose of this study is to accurately model *in vivo* interstitial pressures with a poroelastic model and appropriate boundary conditions. The boundary conditions, meshes, and property designations were systematically varied to isolate the influence of the three features (dural septa, ventricle boundary condition, and saturation parameters) which reflect the creation of four models: 1) the full anatomical model description, 2) the full anatomical description except for dural septa, 3) the full anatomical description but without the ventricle boundary description, and 4) the full anatomical description with fully saturated brain tissue (α=1, $\frac{1}{S} = 0$). The boundary conditions within the context of each model in this study are explained below.

Full Anatomical Condition Description

The full anatomical condition description accounts the model containing full realization of dural septa, ventricles, and heterogeneous hydraulic conductivity and saturation constants. In this realization, the inverse model determines the 6 degrees-of-freedom associated with the material properties that best fits the measured interstitial pressure dynamics during loading. The six properties are $k_{grey\ matter}$, $k_{white\ matter}$, $\alpha_{grey\ matter}$,

$\alpha_{white\ matter}$, $1/S_{grey\ matter}$, and $1/S_{white\ matter}$. Allowing variable saturation parameters does allow a compliance in the fluid component to exist. The far-field (from mechanical load) cortical surfaces are designated as fixed in displacement and experiencing no fluid drainage (Miga et al., 2000). This decision is supported by the dura being left intact during the experiment. The brain stem region is set as stress-free and does not permit fluid drainage. Locations directly associated with the application of piston loading are designated displacement boundary conditions associated with 8 mm, 10 mm, and 12 mm (Miga et al., 2000), and no drainage. The region surrounding the piston area is stress-free and does not allow fluid drainage. This creates a tenting area around the immediate application of the piston (Miga et al., 2000). Consistent with the anatomical role of the dural septa, the nodes associated in the mesh are fixed in displacement and do not permit fluid drainage. In clinical practice, the intracranial pressure reference point is defined at the level of the foramen of Monro (Freeman, 2015). This structure is the part of the ventricles which connects the third and lateral ventricles. Additionally, the ventricular system is continuous with the central spinal canal (Siegel and Sapru, 2015). We hypothesize that this connection permits the ventricles, when the integrity of the dura is not compromised, to act as a reference pressure for the brain. As the ventricles represent a compliant internal boundary that can drain upon loading, while allowed to deform, the pressure at its boundary is set to zero, and it serves as a reference pressure for the rest of the brain. The solution of this set of conditions incorporates the influence of the dural septa, the ventricles, and the sulci and gyri within the brain. In order to isolate and study the influence of all of these individual features, they are then systematically removed with the next three models below.

Condition without Dural Septa Description

To study dural septa influence, a model is created that eliminated the dural septa and its associated boundary condition from the aforementioned model. Similar to the full anatomical model, this model still attempts to determine the same six material properties, namely, $k_{grey\ matter}$, $k_{white\ matter}$, $\alpha_{grey\ matter}$, $\alpha_{white\ matter}$, $1/S_{grey\ matter}$, and $1/S_{white\ matter}$.

Condition without Ventricle Boundary Description

This simulation is done to define the influence of the ventricle boundary condition, which in the full anatomical model serves as a constant pressure reference. In this case, the mesh includes the dural septa split, and its associated boundary conditions. However, the ventricles are now not prescribed a reference pressure, rather they are considered non-draining surfaces. It is still necessary to designate a reference pressure for equation resolution. In this model, we revert back to a previous representation whereby the brain stem nodes are changed from non-draining to a constant pressure of zero, as a reference. We should note that this brain stem designation has been used in other studies (Miga et al., 2000). Similar to the above, the six material properties being fit are $k_{grey\ matter}$, $k_{white\ matter}$, $\alpha_{grey\ matter}$, $\alpha_{white\ matter}$, $1/S_{grey\ matter}$, and $1/S_{white\ matter}$.

Condition Assuming Fully Saturated Tissue Description

The last tissue model is the more traditional model employed when using Biot's consolidation theory to represent brain. Under these indications, the brain is treated as a fully saturated media, resulting in $\frac{1}{S} = 0$ and $\alpha = 1$ for both grey and white matter (Chen et al., 2011), (Miga et al., 2000). This reduces our parameterization fit to only two material properties, $k_{grey\ matter}$ and $k_{white\ matter}$. In the former three models, we allow for unsaturated effects as a means to accommodate missing structural compliance associated with sulci and gyri. In this model, we distinctly terminate that capability in favor of the more common assumptions in the literature.

Inverse Model

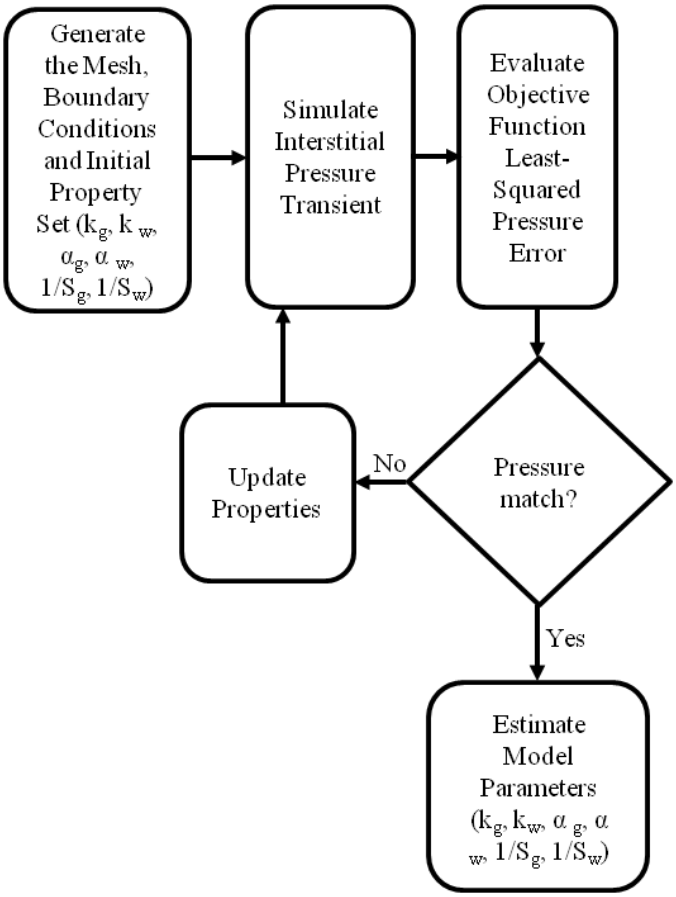

Figure 2. This flow chart illustrates the inverse model used to fit the model calculated intracranial pressure to the experimentally measured intracranial pressure while estimating the material properties.

As alluded to in the previous sections, the general analysis to be achieved in this work is to take each of our models with varying structural and material representations, and reconstruct the material properties to best fit our measured interstitial pressure values form our experimental system. The general structure of this procedure can be seen in Fig. 2. The parameters ($k_{grey\ matter}$, $k_{white\ matter}$, $\alpha_{grey\ matter}$, $\alpha_{white\ matter}$, $1/S_{grey\ matter}$, and $1/S_{white\ matter}$) are estimated with this inverse model approach. The same procedure is applied with all four brain models with the exception that in the last model, only the hydraulic conductivity parameters are reconstructed. In order to ensure repeatability of our results, for each piston push of each inverse reconstruction, twenty randomized initial starting property guesses of the inverse model are performed. Therefore, in this investigation there are a total of 240 distinct runs of the inverse model (4 models, 3 different piston pushes, and 20 initial guesses for each). The 20 distinct initial guesses are generated by randomly perturbing each value of a known fitted property set by +/- 25%.

These randomized property values are input into the poroelastic, finite element model, along with the appropriate boundary conditions, the time step, and the mesh. The interstitial pressure transient is then solved for, and fit to the measured interstitial pressure at the two transducers using a nonlinear least-squares constrained optimization in MATLAB (MathWorks Inc, Nattick, MA). Within our custom objective function, we designate the difference between the model calculated and experimentally measured pressures to be a relative sum-squared error (SSE). The relative sum-squared error is calculated with:

$$SSE = \sum_{i=1}^{i=N} \left(\frac{(P_e - P_m)}{P_e}\right)_i^2 \quad (3)$$

Where P_e is the experimentally measured pressure, P_m is the model determined pressure, and i represents the value of pressure at the i^{th} time point in the transient. Equation (3) represents a relative pressure difference fitting. Given the nature of a step response in interstitial pressure upon surgical loading, this relative measure was used to not unduly weight the early transient pressure values.

With respect to (3), the experimental data consists of 200 data points (100 per transducer) evenly sampled along the time course being modeled. To prevent influence of transducer noise, the experimental values are fit to a fourth order polynomial to the filtered experimental data. With respect to simulation transient, intra-time point values are linearly interpolated to fully utilize the experimental data. Using MATLAB's (MathWorks Inc., Natick MA) trust region reflective optimization framework, property values are iteratively determined such that the least squared error described in (3) is minimized. We use a custom convergence criteria for the optimization, designating that if the difference between 12 consecutive relative sum-squared errors is less than 1E-8, the optimization is complete. The sum-squared error in equation (3) is used as a measure of quality in the model fit.

Once convergence for each of the 240 runs has been achieved, we perform a forward solve of the poroelastic model using the estimated model parameters from each. These forward runs provide both the interstitial pressure and displacement solutions for all runs. We designate two types of results. First, the 'best fit' is the 1 run out of 20 for a specific piston push in a given simulation which converges with the smallest sum-squared error. Second, since 20 pressure profiles for each piston push and model were performed to test for sensitivity to initial guess, the 'average pressure result' represents an average reconstruction value given some arbitrariness to initial guess.

CHAPTER III

RESULTS

Pressure

We use both a qualitative and quantitative analysis to assess the interstitial pressure calculated. In Fig. 3, the results of the inverse model simulations are summarized. The experimental interstitial pressures at both

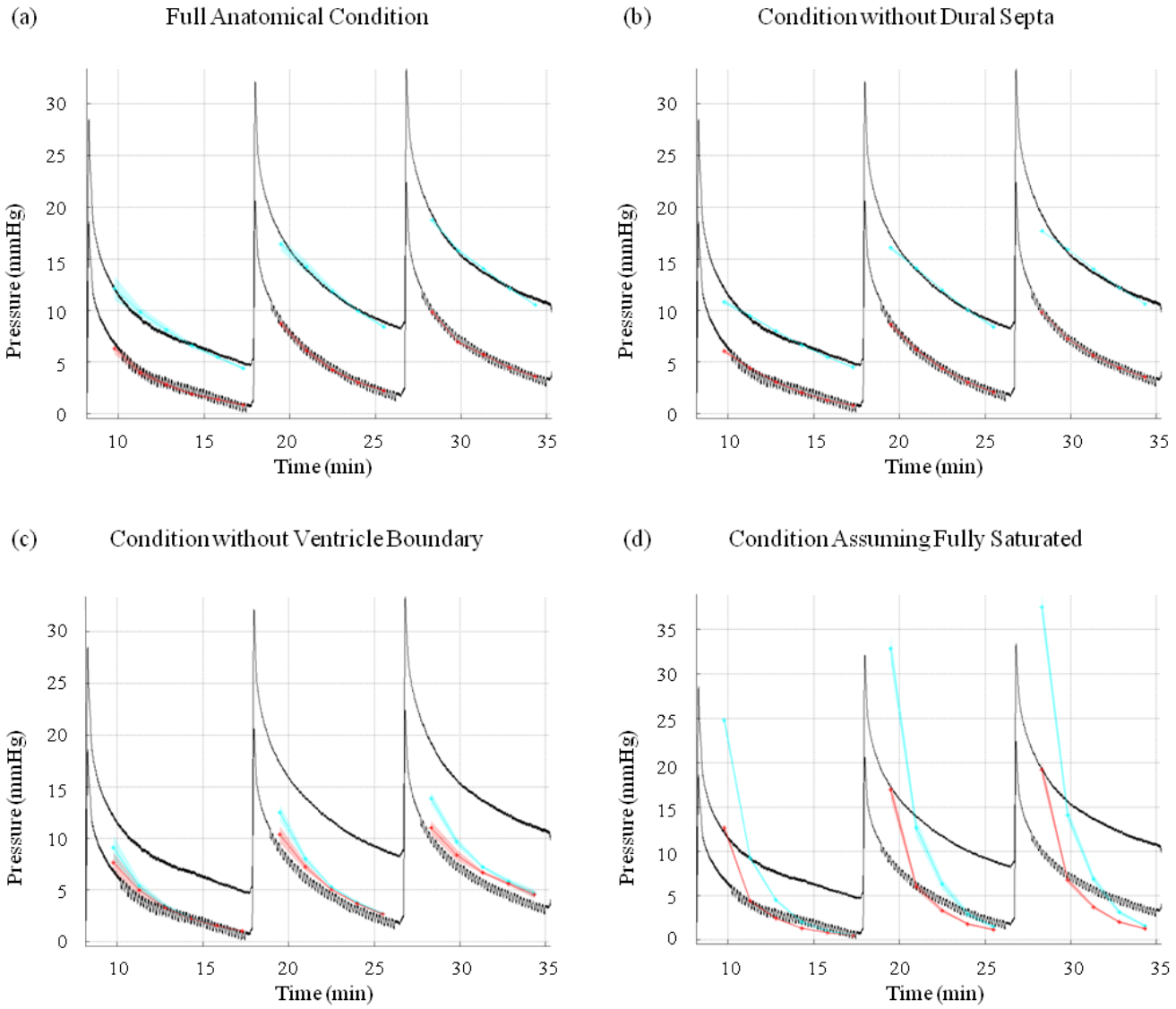

Figure 3. In panels (a), (b), (c), and (d), the solid black lines are the experimental pressure data measured with the transducers. The solid cyan and red lines are the average pressure results in the near hemisphere transducer and far hemisphere transducer respectively. The translucent red and cyan areas are plus and minus two standard deviations of the average pressure result calculated at each time point. Panel (a) shows the model calculated pressure fits obtained when the full anatomical condition is enforced. Panel (b) shows the model calculated pressure fits when the dural septa is not included. Panel (c) show the model calculated pressure fits when the ventricle boundary condition is not included. Panel (d) shows the model calculated pressure fits when the brain tissue is treated as fully saturated.

transducers are shown by the solid, black lines. The higher pressures are associated with the transducer in the hemisphere ipsilateral to the piston. The lower pressures are associated with the transducer in the hemisphere contralateral to the piston push. Observing the measured *in vivo* interstitial pressure, there is a sustained gradient between the two hemispheres of the brain and a distinct transient behavior. In all panels of Fig. 3, the cyan and red lines represent the average pressure results in the transducer which is in the hemisphere ipsilateral to the piston and the transducer which is in the contralateral hemisphere respectively. The shaded regions represent plus and minus two standard deviations of the average pressure results, where the average is associated with the variable initial guess within the parameter determination. From the standard deviations in all panels of Fig. 3, it is evident that the methods used in this investigation provide repeatable results. Panel (a), which is the simulation when all anatomical conditions are enforced, shows that the anatomical specificity enforced captures the amplitude, the gradient between the hemispheres, and the transient. The simulation shown in panel (b) differs from the full anatomical simulation by not including the dural septa representation. Panel (b) shows that the quality of pressure fits in this simulation condition is comparable to the simulation with all of the anatomical constraints enforced. It does, however, consistently have less accuracy at the first time step (90 s) in each piston push relative to the full anatomical description. The simulation in panel (c) differs from the full anatomical simulation by treating the brain stem as the reference pressure of the brain versus the ventricle boundary within the parenchyma. Not only does this result in inaccurate pressure magnitudes, but also does not maintain a sustained gradient between the two transducers. The simulation in panel (d) differs from the full anatomical simulation by treating the brain tissue as a fully saturated material. Initially there is a gradient present between the two transducers, but this gradient is not sustained over the time course of the piston pushes. Additionally, the pressure is overestimated in all of the solutions.

Using the Wilcoxon rank sum test, we compare the set of sum-squared errors obtained in every fit calculated. More specifically, we compare the sum-squared errors of the final solution of each model type to one another to determine if there are statistically relevant differences between each type of model. This test shows that the pressure solutions of the full anatomical description, the description without the dural septa, the description without the ventricle boundary, and the description treating the brain as fully saturated are all statistically significantly different from one another. Based on the difference between the measured *in vivo* pressures and the model estimated pressures, the best pressure fit is associated with the dural septa not being included, but the full description of the boundaries is statistically comparable when evaluating the 12 mm piston push. The lack of ventricle boundary conditions produces a dramatic decrease in the quality of fit, and the treatment of the brain as a saturated medium results in the worst fit, with respect to average sum-squared error, within this investigation.

Qualitatively, the compartmentalization of the interstitial pressure can be visualized in Fig. 4. In Fig. 4, all of the images are of the best fit in each simulation at the 10 mm piston push. These are also all from the first time step in these solutions. Due to the variability in magnitude of the pressure solutions between simulation types, the images were all individually scaled to capture the relative distribution of pressure within the mesh in each simulation. In panel (a), when the full anatomical conditions are accounted for, there are higher pressures in the hemisphere ipsilateral to the piston. There is also a clear distinction between the pressure within the ipsilateral hemisphere relative to the contralateral hemisphere and cerebellum. When the dural septa were not included, there was no compartmentalization between hemispheres or structures present, shown in panel (b). When the brain stem was treated as the reference pressure instead of the ventricles, compartmentalization between the two hemispheres and the cerebrum and cerebellum is still visually evident, shown in panel (c). The extent of the difference between the hemisphere ipsilateral to the piston push and the hemisphere contralateral to the piston push is less distinct than when the full anatomical condition is enforced. In panel (d), where the simulation treats the brain as fully saturated, there is an obvious compartmentalization effect between the ipsilateral and contralateral hemispheres. The area of high pressure is far more pervasive relative to the other simulations. Additionally there are higher pressures present in the cerebellum and brain stem region.

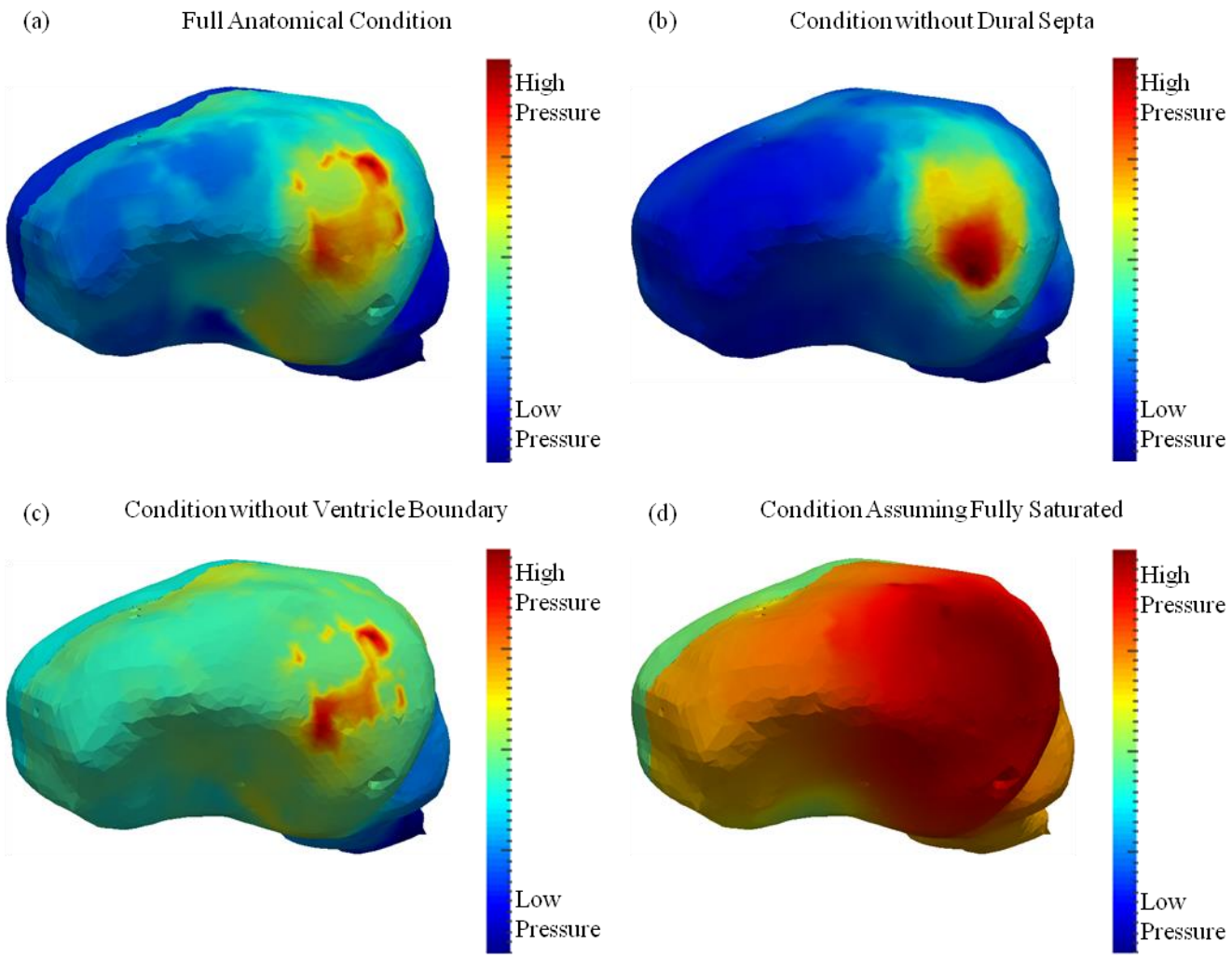

Figure 4. This reflects the differences in compartmentalization based on the type of simulation. In panels (a), (b), (c), and (d), the pressure values are scaled to the minimum and maximum of the specific solutions shown above. The solutions shown above are all the best fits respectively from the first time step of the 10 mm piston push. Panel (a) reflects the compartmentalization when all anatomical conditions are simulated. Panel (b) visualizes the compartmentalization when the dural septa is not included. Panel (c) reflects the compartmentalization when the ventricle boundary condition is not enforced. Panel (d) demonstrates the compartmentalization when the brain tissue is treated as fully saturated.

Shift Correction

As described in the *Methods*, there were stainless steel beads implanted into the parenchyma that were tracked with repeat CT-imaging. Since the inverse model is fit to the experimental interstitial pressure, the displacement of the stainless steel beads provides a source of validation for the simulations performed. They also quantify the quality of the fits for the solid component of the brain tissue. During the experiment, the bead locations were measured at the conclusion of each of the piston pushes. As a metric for comparing displacements, we calculated the percent shift correction at the conclusion of the 8 mm, 10 mm, and 12 mm piston push in each simulation performed (Table 2). The runs evaluated were the best fits for each of the piston pushes and simulations respectively. The percent shift correction is calculated using Eq. 4 below.

$$\%Correction = 100\% * \left(1 - \frac{mean(\|\overrightarrow{d_e} - \overrightarrow{d_m}\|)}{mean(\|\overrightarrow{d_e}\|)}\right) \quad (4)$$

Where $\overrightarrow{d_e}$ is the experimentally measured displacement vector, and $\overrightarrow{d_m}$ is the model determined displacement vector. Table 2 shows that the best shift correction is consistently accomplished when the dural septa boundary is not included.

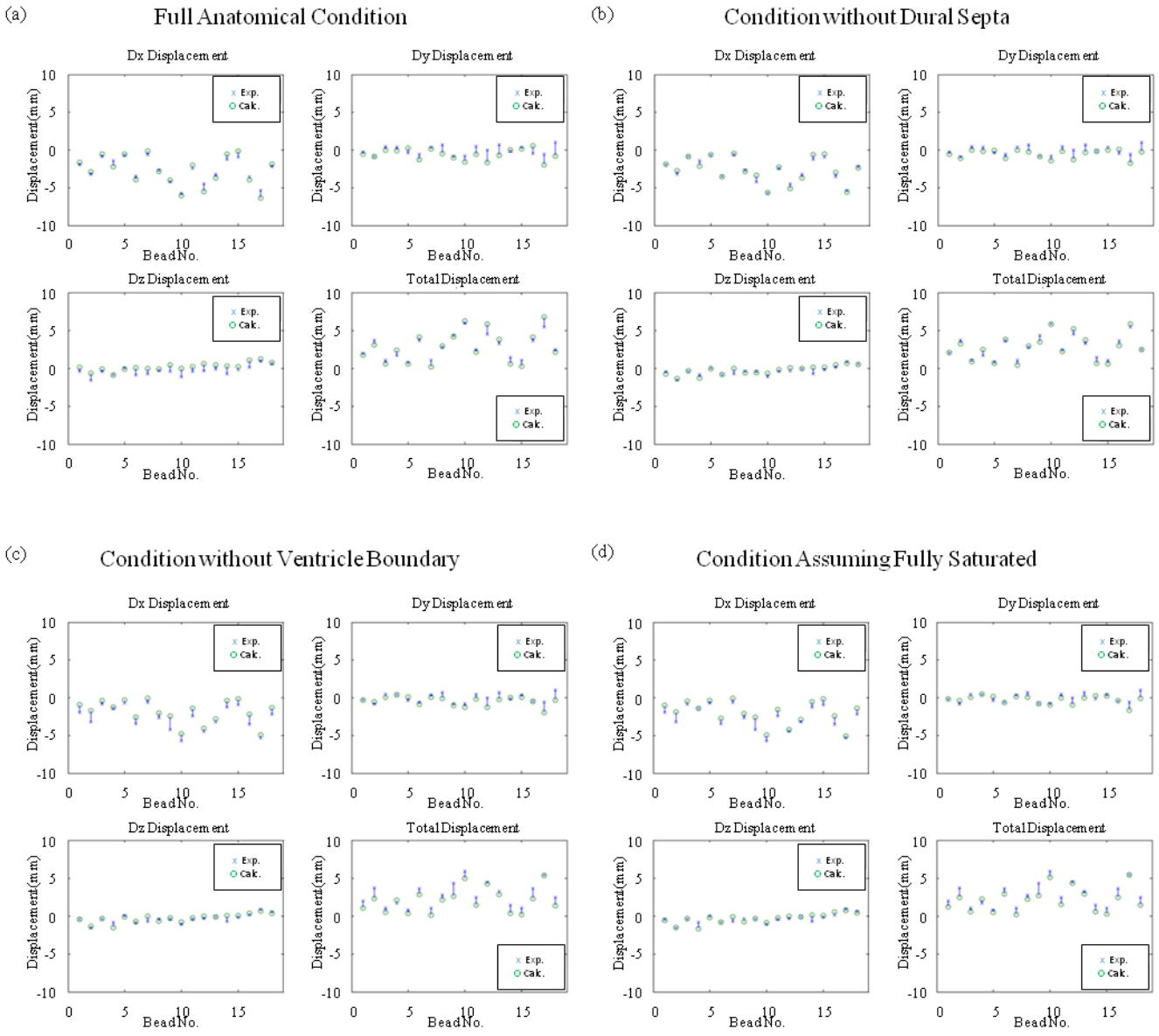

Figure 5. These are calculations from the best fits runs from the 10 mm piston push. These calculations quantify the model calculated (Calc.) bead displacements at the conclusion of the simulated piston push and compare them to the experimentally (Exp.) measured displacements. In panels (a), (b), (c), and (d) the top left, top right, and bottom left subfigures are the displacement calculations in the x, y, and z axis respectively. The subfigure on the bottom right of all the panels represents the total displacement.

Looking more specifically at the individual bead displacements at the 10 mm piston push, which reflects the general behavior between the shift corrections, the same trend was reflected (Fig. 5). The strongest agreement between the experimental (Exp.) and model calculated (Calc.) bead displacements are present in the simulation

which excluded the dural septa (Fig. 5 panel (b)). The full anatomical description, shown in panel (a), also was able to reasonably approximate the bead displacements. Comparing all panels, it is evident that all of the models were able to calculate shift corrections comparably.

TABLE 2
PERCENT SHIFT CORRECTION

PERCENT SHIFT CORRECTION		**Piston Push**		
		8 mm	10 mm	12 mm
Simulation	Full Anatomical Condition	60.0	57.6	53.7
	Condition without Dural Septa	64.5	70.3	73.8
	Condition without Ventricle Boundary	58.1	60.2	64.8
	Condition Assuming Fully Saturated	60.0	65.0	67.4

Evaluating the same set of piston pushes shown in Table 2, we use the Wilcoxon rank sum test to determine if the quality of displacement fits is statistically different between simulations. For each simulation type and piston push, $\|\overrightarrow{d_e} - \overrightarrow{d_m}\|$ for the 18 beads is calculated for the run with the smallest sum-squared error. Then the simulations are compared to one another with respect to these sets of measurements (18 beads at every piston push). Although some piston specific comparisons revealed statistical significance, these differences were not present in every piston push comparison. Therefore, we are unable to conclusively say that the shift corrections between the simulations are statistically significantly different from one another. Therefore, the shift correction accomplished in all simulations are of comparable quality.

Property Reconstruction

From Fig. 3 it is clear that the quality of the fits was not highly variable between the repeated initializations of our inverse problem framework. Despite this, we did notice some degree of variability between the properties reconstructed within the groups of runs. Table 3 shows the properties found in the best fits. The property values estimated for grey and white matters are consistently different across all of the best fit properties across all piston pushes and simulations. This would suggest that including heterogeneity was a necessary condition to capture best fits. Observing the changes in the best fits of $k_{grey\ matter}$ and $k_{white\ matter}$ in the full anatomical conditions, conditions without the dural septa, and conditions excluding the ventricle boundary, there is a change in the magnitude with piston push changes however we see a consistent behavior where the hydraulic conductivity associated with white matter is greater than that of grey. Although not true for every best fit, $\alpha_{white\ matter}$ tends to be closer to the historical value of 1, which corresponds to the brain tissue treated as a saturated material. This

is in contrast to $\alpha_{grey\ matter}$, which is generally lower. Table 3 reflects different property values based on the simulation selected. The reconstructions of $1/S_{grey\ matter}$ and $1/S_{white\ matter}$ were all non-zero, regardless of simulation type. Additionally, the variations between runs not only change among simulation types, but also between the properties themselves.

TABLE 3
ESTIMATED PROPERTIES SUMMARY

Simulation	Piston Push	k_g Best Fit	k_w Best Fit	α_g Best Fit	α_w Best Fit	$1/S_g$ Best Fit	$1/S_w$ Best Fit
Full Anatomical Condition	8 mm	2.7E-13	1.9E-11	4.3E-01	8.7E-01	3.3E-06	4.3E-05
	10 mm	3.2E-13	1.1E-11	4.5E-01	5.8E-01	2.6E-06	3.0E-05
	12 mm	1.8E-12	9.8E-12	4.8E-01	1.0E+00	2.3E-06	4.4E-05
AVERAGE		8.0E-13	1.3E-11	4.5E-01	8.2E-01	2.7E-06	3.9E-05
Condition without Dural Septa	8 mm	2.2E-14	8.0E-12	3.9E-03	8.8E-01	5.5E-10	2.2E-05
	10 mm	2.5E-14	2.8E-12	4.9E-03	4.2E-01	1.1E-13	9.1E-06
	12 mm	4.2E-14	9.0E-13	5.9E-03	1.8E-01	2.8E-11	4.7E-06
AVERAGE		3.03-14	3.9E-12	4.9E-03	4.9E-01	1.9E-10	1.2E-05
Condition without Ventricle Boundary	8 mm	5.9E-12	1.1E-09	4.5E-01	8.5E-01	1.5E-07	3.0E-05
	10 mm	1.7E-12	1.3E-09	1.0E+00	7.9E-01	4.9E-06	4.5E-05
	12 mm	1.0E-12	8.4E-10	7.2E-01	9.8E-01	3.4E-06	5.6E-05
AVERAGE		2.9E-12	1.1E-09	7.2E-01	8.7E-01	2.8E-06	4.4E-05
Condition Assuming Fully Saturated	8 mm	9.0E-11	1.0E-12	-	-	-	-
	10 mm	8.2E-11	1.0E-12	-	-	-	-
	12 mm	8.7E-11	1.0E-12	-	-	-	-
AVERAGE		8.6E-11	1.0E-12				

CHAPTER IV

DISCUSSION

The pressure results shown in Fig. 3 panels (a) and (b) reflect that the interstitial pressure can be modeled using the full anatomical description as well as the description which did not include the dural septa. While the significance of removing the dural septa boundary was not evident in Fig. 3, comparing the pressure distributions between panel (b) and the remaining panels of Fig. 4, it is evident that it defines the compartmentalization of pressure between the left and right hemispheres as well as between the cerebrum and cerebellum. Further investigation with multiple pressure transducers is needed to properly tune the compartmentalization effect. The percent shift correction when the dural septa are excluded is consistently better than the other simulations (Table 2 and Fig. 5). While this was an unexpected result, it may be due to the manner in which the dural septa boundary conditions were implemented, i.e. it is possible that the use of Dirichlet conditions for septal nodes may be over constraining the solution. Moreover, the shift corrections were not statistically significantly different than the other model calculated shift corrections at every piston push.

Excluding the ventricle boundary condition resulted in a substantially worse result, which is reflected by inaccurate pressure magnitudes. The results of Fig. 3 panel (c) in conjunction with the results of Fig. 4 panel (c) also indicated that the pressures in both the hemispheres ipsilateral and the contralateral to the applied piston push were very similar in magnitude. This provides evidence that the appropriate treatment of the ventricle boundary within the parenchymal tissue can have significant effect on biomechanical models of the brain. Our decision to treat the boundary as a reference model in the brain came from the clinical practice which treats the level of the foramen of Monro as the intracranial pressure zero point (Freeman, 2015). The percent shift correction in this simulation was also comparable to the other simulations in this paper (Table 2 and Fig. 5).

Treating the brain as a fully saturated tissue, shown in Fig. 3 panel (c), is the current convention for poroelastic models (Chen et al., 2011), (Miga et al., 2000). With this in mind, our results indicate that this may not be the appropriate description of the brain tissue. The magnitudes of the experimental data were not matched, and the gradient between the hemispheres is not sustained. The differences between panels (a) and (d) reflect that enabling the brain tissue to be unsaturated yields a substantial improvement in quality of fit. The results of the percent shift correction are also comparable to the full anatomical description (Table 2 and Fig. 5). In a previous study of volume regulation, the results led to a hypothesis that brain interstitial space could possibly experience volume variations based on stresses present (Doczi, 1993). It is not definite what phenomena the saturation property terms are capturing, but we hypothesize that they may be acting as a bulk additional fluid compliance resulting from the ready evacuation of fluid from fissures and sulci spaces into subarachnoid spaces during compression.

The properties we estimated in the four simulations are discernably different. This speaks to the variability of literature on quantifying brain material properties. While not the focus of this paper, we reconstructed four categories of material properties associated with the poroelastic model with varying boundary condition and mesh configurations. We also observed changes in magnitude of hydraulic conductivity between different extents of piston application. In the context of a single pig, described four different ways, we are able to find a range of estimated brain tissue properties. This speaks to the need to use literature property values which were gathered in a method most congruent with the biomechanical investigation being performed.

One shortcoming of the work is in regards to the instrumentation extent. Ultimately, our inverse model is driven by two transducer measurements. To some degree, this is a lack of specificity in the raw data, and it is a likely contributor to the considerable differences between the minimum and maximum property estimates within the sets of 20 runs per simulation per piston translation. We could add specificity by increasing our fitting dimensionality with bead displacement data. We should note that we did consider this. We elected not to do this

because this would ultimately require a weighting framework which we though could also contribute to property reconstruction variability. Nevertheless, this will be a future investigation.

Our full anatomical description simulation in conjunction with the poroelastic model is able to accurately model *in vivo* interstitial pressures and tissue deformation. It also reflects the compartmentalization of interstitial pressure within different areas of the brain. The presence of our treatment of the ventricles and brain tissue as unsaturated has a significant impact on the accuracy of the results, while the presence of the dural septa is less essential for the purposes of this investigation and may have influenced results by being over constrained. Based on the results of the simulation with the full anatomical description, we also infer that our choice to incorporate heterogeneity with grey and white matters was appropriate. Lastly, this work challenges the conventional representation of the poroelastic model in brain mechanics with a sound *in vivo* data-driven methodology and demonstrates that common assumptions in poroelasticity need to be questioned in the face of complex anatomical interactions.

CHAPTER V

CONCLUSION

The purpose of this investigation is to accurately model *in vivo* interstitial pressures, determine the anatomical specificity necessary to capture the pressures accurately, and to estimate the material property values of the brain. The results of this study provide strong evidence for the use of a poroelastic representation of brain tissue and the pivotal role that certain anatomical features play in accurately modeling both pressure and deformation of brain tissue. To the best of our knowledge, the model reconstructions in the simulation with a full anatomical description has not been accomplished in other studies into modeling *in vivo* work. This work highlights the importance of incorporating features, such as tissue heterogeneity, the ventricles, and the dural septa in future biomechanical models of the brain. The work also challenges conventional assumptions regarding poroelastic theory applied to brain biomechanics. While we cannot conclusively say that the need to add fluid-compliance is explained by the evacuation of intra-sulci/intra-fissure fluid into subarachnoid spaces, it is evident from this research that their addition to the model results in the accurate capturing of interstitial pressure magnitudes, transient behavior, and importantly the spatial gradient – effects that were very challenging to capture in past modeling efforts.

REFERENCES

AMESTOY, P. R., DUFF, I. S., L'EXCELLENT, J.-Y. & KOSTER, J. 2001. A Fully Asynchronous Multifrontal Solver Using Distributed Dynamic Scheduling. *SIAM Journal of Matrix Analysis and Applications,* 23**,** 15-41.

AMESTOY, P. R., GUERMOUCHE, A., L'EXCELLENT, J.-Y. & PRALET, S. 2006. Hybrid Scheduling for the Parallel Solution of Linear Systems. *Parallel Computing,* 32**,** 136-156.

BALAY, S., ABHYANKAR, S., ADAMS, M. F., BROWN, J., BRUNE, P., BUSCHELMAN, K., DALCIN, L., EIJKHOUT, V., GROPP, W. D., KAUSHIK, D., KNEPLEY, M. G., MCINNES, L. C., RUPP, K., SMITH, B. F., ZAMPINI, S., ZHANG, H. & ZHANG, H. 2016a. PETSc Users Manual. *In:* LABORATORY, A. N. (ed.).

BALAY, S., ABHYANKAR, S., ADAMS, M. F., BROWN, J., BRUNE, P., BUSCHELMAN, K., DALCIN, L., EIJKHOUT, V., GROPP, W. D., KAUSHIK, D., KNEPLEY, M. G., MCINNES, L. C., RUPP, K., SMITH, B. F., ZAMPINI, S., ZHANG, H. & ZHANG, H. 2016b. *PETScWeb page* [Online]. Available: http://www.mcs.anl.gov/petsc [Accessed].

BALAY, S., GROPP, W. D., MCINNES, L. C. & SMITH, B. F. 1997. Efficient management of parallelism in object oriented numerical software libraries, in: Modern Software Tools in Scientific Computing. Birkhauser Press.

BIOT, M. A. 1941. General Theory of Three-Dimensional Consolidation. *Journal of Applied Physics,* 12**,** 155-164.

CHATELIN, S., CONSTANTINESCO, A. & WILLINGER, R. 2010. Fifty years of brain tissue mechanical testing: from in vitro to in vivo investigations. *Biorheology,* 47**,** 255-76.

CHEN, I., COFFEY, A. M., DING, S., DUMPURI, P., DAWANT, B. M., THOMPSON, R. C. & MIGA, M. I. 2011. Intraoperative brain shift compensation: accounting for dural septa. *IEEE Trans Biomed Eng,* 58**,** 499-508.

CLATZ, O., DELINGETTE, H., TALOS, I. F., GOLBY, A. J., KIKINIS, R., JOLESZ, F. A., AYACHE, N. & WARFIELD, S. K. 2005. Robust nonrigid registration to capture brain shift from intraoperative MRI. *IEEE Trans Med Imaging,* 24**,** 1417-27.

COFFEY , A. M., MIGA , M. I., CHEN , I. & THOMPSON, R. C. 2013. Toward a preoperative planning tool for brain tumor resection therapies. *Int J CARS,* 8**,** 87–97.

DAI, W., ASTARY, G. W., KASINADHUNI, A. K., CARNEY, P. R., MARECI, T. H. & SARNTINORANONT, M. 2016. Voxelized Model of Brain Infusion That Accounts for Small Feature Fissures: Comparison With Magnetic Resonance Tracer Studies. *J Biomech Eng,* 138**,** 051007.

DELORENZO, C., PAPADEMETRIS, X., STAIB, L. H., VIVES, K. P., SPENCER, D. D. & DUNCAN, J. S. 2012. Volumetric intraoperative brain deformation compensation: model development and phantom validation. *IEEE Trans Med Imaging,* 31**,** 1607-19.

DOCZI, T. 1993. Volume Regulation of the Brain Tissue-a Survey*. *Acta Neurochirurgica,* 121**,** 1-8.

FERRANT , M., NABAVI , A., MACQ, B., BLACK , P. M., JOLESZ , F. A., KIKINIS , R. & WARFIELD, S. K. 2002. Serial registration of intraoperative MR images of the brain. *Medical Image Analysis,* 6**,** 337–359.

FREEMAN, W. D. 2015. Management of Intracranial Pressure. *Continuum,* 21**,** 1299–1323.

GERARD, I. J., KERSTEN-OERTEL, M., PETRECCA, K., SIRHAN, D., HALL, J. A. & COLLINS, D. L. 2017. Brain shift in neuronavigation of brain tumors: A review. *Med Image Anal,* 35**,** 403-420.

GREEN, M. A., BILSTON, L. E. & SINKUS, R. 2008. In vivo brain viscoelastic properties measured by magnetic resonance elastography. *NMR Biomed,* 21**,** 755-64.

HAGEMANN , A., ROHR, K. & STIEHL, H. S. 2002. Coupling of fluid and elastic models for biomechanical simulations of brain deformations using FEM. *Medical Image Analysis* 6**,** 375–388.

HU, J., JIN, X., LEE, J. B., ZHANG, L., CHAUDHARY, V., GUTHIKONDA, M., YANG, K. H. & KING, A. I. 2007. Intraoperative brain shift prediction using a 3D inhomogeneous patient-specific finite element model. *Journal of Neurosurgery,* 106**,** 164–169.

KARAMI, G., GRUNDMAN, N., ABOLFATHI, N., NAIK, A. & ZIEJEWSKI, M. 2009. A micromechanical hyperelastic modeling of brain white matter under large deformation. *J Mech Behav Biomed Mater,* 2**,** 243-54.

KYRIACOU, S. K., MOHAMED, A., MILLER, K. & NEFF, S. 2002. Brain mechanics For neurosurgery: modeling issues. *Biomech Model Mechanobiol,* 1**,** 151-64.

LIEBERMAN, D. M., LASKE, D. W., MORRISON, P. F., BANKIEWICZ, K. S. & OLDFIELD, E. H. 1995. Convection-enhanced distribution of large molecules in gray matter during interstitial drug infusion. *J Neurosurg,* 82**,** 1021–1029.

LINNINGER, A. A., SOMAYAJI, M. R., MEKARSKI, M. & ZHANG, L. 2008. Prediction of convection-enhanced drug delivery to the human brain. *J Theor Biol,* 250**,** 125-38.

LYNCH, D. R. 2005. *Numerical Partial Differential Equations for Environmental Scientists and Engineers,* New York, NY, Springer Science+Business Media, Inc. .

MIGA , M. I. 1998. *Development and Quantification of a 3D Brain Deformation Model for Model-Updated Image-Guided Stereotactic Neurosurgery.* Ph.D. , Dartmouth College.

MIGA, M. I. 2016. Computational Modeling for Enhancing Soft Tissue Image Guided Surgery: An Application in Neurosurgery. *Ann Biomed Eng,* 44**,** 128-38.

MIGA, M. I., PAULSEN, K. D., HOOPES, P. J., KENNEDY, F. E., HARTOV, A. & ROBERTS, D. W. 2000. In Vivo Modeling of Interstitial Pressure in the Brain Under Surgical Load Using Finite Elements. *Transactions of the ASME,* 122**,** 354-363.

MIGA , M. I., PAULSEN, K. D., HOOPES, P. J., KENNEDY, F. E., HARTROV, A. & ROBERTS, D. W. 2000. In-Vivo Analysis of Heterogeneous Brain Deformation Computations for Model-Updated Image Guidance. *Comput Methods Biomech Biomed Eng,* 3**,** 129-146.

MIGA, M. I., PAULSEN, K. D. & KENNEDY, F. E. 1998. Von Neumann Stability Analysis Of Biot's General Two-Dimensional Theory Of Consolidation. *International Journal For Numerical Methods In Engineering,* 43**,** 955–974.

MIGA, M. I., PAULSEN, K. D., KENNEDY, F. E., HOOPES, P. J., HARTOV, A. & ROBERTS, D. W. 1997. A 3D Brain Deformation Model Experiencing Comparable Surgical Loads. *Proceedings - 19th International Conference - IEEE/EMBS.* Chicago, IL. USA.

MIGA , M. I., PAULSEN, K. D., KENNEDY, F. E., HOOPES, P. J., HARTOV, A. & ROBERTS, D. W. 1998. Modeling Surgical Loads to Account for Subsurface Tissue Deformation During Stereotactic Neurosurgery. *IEEE SPIE Proceedings of Laser-Tissue Interaction IX, Part B: Soft-tissue Modeling.*

MIGA, M. I., ROBERTS, D. W., KENNEDY, F. E., PLATENIK, L. A., HARTOV, A., LUNN, K. E. & PAULSEN, K. D. 2001. Modeling of Retraction and Resection for Intraoperative Updating of Images. *Neurosurgery,* 49**,** 75-85.

MIGA, M. I., SUN, K., CHEN, I., CLEMENTS, L. W., PHEIFFER, T. S., SIMPSON, A. L. & THOMPSON, R. C. 2016. Clinical evaluation of a model-updated image-guidance approach to brain shift compensation: experience in 16 cases. *Int J Comput Assist Radiol Surg,* 11**,** 1467-74.

MILLER, K. 1999. Constitutive model of brain tissue suitable for finite element analysis of surgical procedures. *Journal of Biomechanics,* 32**,** 531-537.

MILLER, K. & CHINZEI, K. 1997. Constitutive Modeling Experiment of Brain Tissue: Experiment and Theory. *Journal of Biomechanics,* 30**,** 1115-1121.

MILLER, K. & CHINZEI, K. 2002. Mechanical properties of brain tissue in tension. *Journal of Biomechanics,* 35**,** 483–490.

MONRO, A. 1783. *Observations on Structure and Functions of the Nervous System*.

MOSTAYED, A., GARLAPATI, R. R., JOLDES, G. R., WITTEK, A., ROY, A., KIKINIS, R., WARFIELD, S. K. & MILLER, K. 2013. Biomechanical model as a registration tool for image-guided neurosurgery: evaluation against BSpline registration. *Ann Biomed Eng,* 41**,** 2409-25.

NIMSKY, C., GANSLANDT, O., CERNY, S., HASTREITER, P., GREINER, G. & FAHLBUSCH, R. 2000. Quantification of, Visualization of, and Compensation for Brain Shift Using Intraoperative Magnetic Resonance Imaging. *Neurosurgery,* 47**,** 1070-1080.

OHUE, S., KUMON, Y., NAGATO, S., KOHNO, S., HARADA, H., NAKAGAWA, K., KIKUCHI, K., MIKI, H. & OHNISHI, T. 2010. Evaluation of Intraoperative Brain Shift Using an Ultrasound-Linked Navigation System for Brain Tumor Surgery. *Neurologia Medico-Chirurgica (Tokyo),* 50**,** 291-300.

PAULSEN, K. D., MIGA, M. I., KENNEDY, F. E., HOOPES, P. J., HARTOV, A. & ROBERTS, D. W. 1999. A Computational Model for Tracking Subsurface Tissue Deformation During Stereotactic Neurosurgery. *IEEE Transactions On Biomedical Engineering,* 46.

PRANGE, M. T. & MARGULIES, S. S. 2002. Regional, Directional, and Age-Dependent Properties of the Brain Undergoing Large Deformation. *Journal of Biomechanical Engineering,* 124**,** 244-252.

RAGHAVAN, R., BRADY, M. L., RODRIGUEZ-PONCE, M. I., HARTLEP, A., PEDAIN, C. & SAMPSON, J. H. 2006. Convection-enhanced delivery of therapeutics for brain disease, and its optimization. *Neurosurg Focus,* 20**,** 1-13.

SACK, I., BEIERBACH, B., HAMHABER, U., KLATT, D. & BRAUN, J. 2008. Non-invasive measurement of brain viscoelasticity using magnetic resonance elastography. *NMR In Biomedicine,* 21**,** 265-71.

SCHROEDER, W., MARTIN, K. & LORENSEN, B. 1996. *The Visualization Toolkit: An Object-Oriented Apprroach to 3D Graphics,* New Jersey, Prentice-Hall.

SCHULZ, C., WALDECK, S. & MAUER, U. M. 2012. Intraoperative image guidance in neurosurgery: development, current indications, and future trends. *Radiol Res Pract,* 2012**,** 197364.

SIEGEL, A. & SAPRU, H. N. 2015. *Essential Neuroscience,* Baltimore, MD, Lippincott Williams & Wilkins.

SULLIVAN, J. M. J., CHARRON, G. & PAULSEN, K. D. 1997. A Three Dimensional Mesh Generator for Arbitrary Multiple Material Domains. *Finite Elem Anal Design,* 25**,** 219-241.

SUN, K., PHEIFFER, T. S., SIMPSON, A. L., WEIS, J. A., THOMPSON, R. C. & MIGA, M. I. 2014. Near Real-Time Computer Assisted Surgery for Brain Shift Correction Using Biomechanical Models. *IEEE J Transl Eng Health Med,* 2.

WITTEK, A., HAWKINS, T. & MILLER, K. 2009. On the unimportance of constitutive models in computing brain deformation for image-guided surgery. *Biomech Model Mechanobiol,* 8**,** 77-84.

WOLFLA, C. E., LUERSSEN, T. G. & BOWMAN, R. M. 1997. Regional brain tissue pressure gradients created by expanding extradural temporal mass lesion. *Journal of Neurosurgery,* 86**,** 505–510.

WOLFLA, C. E., LUERSSEN, T. G., BOWMAN, R. M. & PUTTY, T. K. 1996. Brain tissue pressure gradients created by expanding frontal epidural mass lesion. *Journal of Neurosurgery,* 84**,** 642-647.